Lithium Mechanics: Roles of Strain Rate and Temperature and Implications for Lithium Metal Batteries

William S. LePage,[1] Yuxin Chen,[1] Eric Kazyak,[1] Kuan-Hung Chen,[2,*] Adrian J. Sanchez,[1] Andrea Poli,[1] Ellen M. Arruda,[1,3,4] M. D. Thouless,[1,2] and Neil P. Dasgupta[1,,z]**

[1]*Department of Mechanical Engineering, University of Michigan, Ann Arbor, Michigan 48109, USA*
[2]*Department of Materials Science and Engineering, University of Michigan, Ann Arbor, Michigan 48109, USA*
[3]*Program in Marcomolecular Science and Engineering, University of Michigan, Ann Arbor, Michigan 48109, USA*
[4]*Department of Biomedical Engineering, University of Michigan, Ann Arbor, Michigan 48109, USA*

The lack of a reliable rechargeable lithium metal (Li-metal) anode is a critical bottleneck for next-generation batteries. The unique mechanical properties of lithium influence the dynamic evolution of Li-metal anodes during cycling. While recent models have aimed at understanding the coupled electrochemical-mechanical behavior of Li-metal anodes, there is a lack of rigorous experimental data on the bulk mechanical properties of Li. This work provides comprehensive mechanical measurements of Li using a combination of digital-image correlation and tensile testing in inert gas environments. The deformation of Li was measured over a wide range of strain rates and temperatures, and it was fitted to a power-law creep model. Strain hardening was only observed at high strain rates and low temperatures, and creep was the dominant deformation mechanism over a wide range of battery-relevant conditions. To contextualize the role of creep on Li-metal anode behavior, examples are discussed for solid-state batteries, "dead" Li, and protective coatings on Li anodes. This work suggests new research directions and can be used to inform future electrochemical-mechanical models of Li-metal anodes.

 [DOI: 10.1149/2.0221902jes]

Manuscript submitted November 9, 2018; revised manuscript received December 21, 2018. Published January 8, 2019.

One of the major bottlenecks for next-generation batteries is the ability to replace graphite anodes with lithium metal (Li-metal) anodes, which have the ability to increase the theoretical specific capacity by a factor of 10 (3860 mAh/g) with a highly negative potential (-3.04 V versus the standard hydrogen electrode).[1,2] However, the development of rechargeable Li-metal batteries has suffered from low Coulombic efficiencies, electrochemical instabilities, and evolution of high-surface-area morphologies, including "mossy" Li, "dead" Li, and a range of dendrite morphologies that accelerate cell degradation and lead to safety concerns.[2]

The renewed interest in rechargeable Li-metal anodes has been fueled by advances in both liquid- and solid-electrolyte chemistries, enhanced protective coating strategies, the development of 3D current collector architectures, and improved in-situ/operando methods to identify the fundamental bottlenecks for reversible electrodeposition and dissolution of Li.[1] However, much of the recent work in this area has focused on mitigating symptoms of poor performance, including suppressing non-planar morphologies, measuring Coulombic efficiency of plating/stripping from current collectors, and quantifying critical current densities that lead to internal shorting.[2] This has led to the evolution of a field that is often empirical, rather than a focus on an improved fundamental understanding of underlying mechanisms.

One of the reasons that it is difficult to identify and quantify the root cause of poor performance is that rechargeable Li-metal anodes are not static, homogeneous electrodes. Rather, they evolve dynamically during electrodeposition and stripping, often with dramatic changes in electrode volume, surface area, morphology, and solid-electrolyte interphase (SEI) properties.[3] In particular, there is an increasing consensus that the mechanical properties of Li play an important role in morphological evolution, including the nucleation and growth of dendrites,[4] the propagation of Li through solid electrolytes,[5,6] the mechanical detachment of metallic Li from the electrode surface ("dead Li" formation),[7] and the mechanical failure of protective membranes on the Li surface.[8] To overcome these challenges, it is critical to increase our knowledge of the coupled electrochemical, mechanical, and morphological behavior of Li, and how it evolves during cycling under a wide range of conditions.[9]

The pioneering work of Monroe and Newman[10] proposed a model for dendrite propagation at a Li/polymer interface. It was proposed that the growth of these dendrites is driven by the distribution of elastic stresses at the interface, and that dendrites are suppressed when the shear modulus of the polymer is approximately twice that of Li. The model assumed that the Li behaves as a linear-elastic solid, which limits the range of conditions under which it is applicable, since bulk Li has a very low yield strength.

To build upon this foundation, the linear-elastic model[10] has been extended to account for plasticity.[4,11] Owing to the limited availability of mechanical property data on bulk Li, the mechanical properties of Li were represented without the effects of temperature or strain rate. However, the mechanical properties of Li have a strong dependence on strain rate and temperature, owing to a low melting temperature of 453 K, which corresponds to a homologous temperature of $T_H = 0.65$ at 298 K. In addition, the low activation energy for self-diffusion in solid Li (50 kJ mol^{-1})[12,13] indicates that significant creep of Li will occur at room temperature. This illustrates the need for a comprehensive set of experimental data on the plasticity and creep properties of Li to inform models that predict its coupled electrochemical-mechanical behavior.

There are relatively few experimental reports of the mechanical properties of bulk Li. A study of Li compression reported yield stresses for temperatures between 4.2 and 80 K at one strain rate.[14] Also, the critical resolved shear stresses in single-crystal Li were measured between 78 and 400 K at one strain rate.[15] In another set of studies, the bulk mechanical properties of Li were measured at relatively fast strain rates (2×10^{-3} to 1 s^{-1}) for temperatures between 295 and 348 K. These conditions were likely chosen due to the non-battery application of the study (a collection lens for an antiproton source).[16,17] In addition, the creep deformation of Li has been reported using constant-force measurements at room temperature.[18–20]

Nano-mechanical experiments have been performed to probe the deformation of Li in compression at small length scales. These have included nano-indentation,[21–24] micro-pillar compression,[25] and atomic force microscopy.[26] These localized surface measurements provide valuable insights into Li-metal deformation at the nanoscale, especially by pointing to length-scale effects that are significant when Li is confined to small dimensions. Along with these small-scale observations, there is a need for a complementary data set on the bulk mechanical response of polycrystalline Li, as suggested in recent modeling work.[27] These data could then be used to inform continuum-scale

*Electrochemical Society Student Member.
**Electrochemical Society Member.
zE-mail: ndasgupt@umich.edu

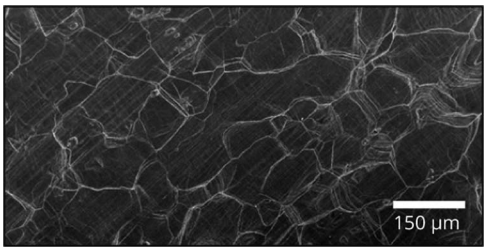

Figure 1. SEM image of Li foil surface microstructure.

models of Li deformation under varying stack pressures, strain rates, and temperatures.

This paper presents measurements for the mechanical properties of bulk Li using battery-grade foils in inert gas environments. The deformation of Li was investigated over a wide range of strain rates (2×10^{-5} to 2×10^{-2} s^{-1}) and temperatures (198 to 398 K), which were used to calibrate a power-law creep model. Strain hardening was only observed at high strain rates and low temperatures. The results demonstrate that creep is the dominant deformation mechanism over a significant range of battery-relevant conditions. Finally, the Discussion of this report contextualizes the implications of these results on the coupled electrochemical-mechanical behavior of Li-metal anodes against both solid and liquid electrolytes. The impact of this work is intended to bridge the electrochemistry and solid mechanics communities in a new way, both by providing a more comprehensive and well-controlled set of experimental data on the mechanical properties of Li, and by demonstrating knowledge gaps that can be filled when equipped with these results.

Experimental

Materials.—All experiments used battery-grade Li foil (99.9% metals basis, packed in Ar, Alfa Aesar). The as-received foils were characterized by scanning electron microscopy (SEM; Mira3 field-emission gun, Tescan), and the average surface grain size was 150 μm based on the area of 60 grains (Figure 1).

The crystallographic texture of the foils (Figure 2) was measured with in-plane X-ray diffraction (Cu-Kα source; SmartLab, Rigaku) and plotted with MTEX.[28] Consistent with previous results,[29] the rolled Li foils exhibited a preferential [100] out-of-plane orientation, with no preferred in-plane texture (Figure 2a). All tensile samples were prepared with the axial direction in the plane of the foil. To confirm that the tensile response of the Li was isotropic in the plane of the foil, tensile experiments were performed in the rolling and transverse directions, and identical stress-strain behaviors were observed (Figure 2b).

Methods for strain-rate dependent deformation.—A new platform was developed for measuring the deformation of air-sensitive solids using 3D digital-image correlation (DIC) (Figure S1). In this work, the platform was used to study strain-rate effects for the deformation of Li (Results of strain-rate dependent deformation section). The experimental platform consisted of an Ar glove box, a custom-designed, mechanical-testing system (inside the glove box), and two machine-vision cameras (PointGrey GRAS 50S5M-C) with 75 mm lenses (Fujinon HF75SA-1) and 40 mm extension tubes. The cameras were positioned outside the glove box on a rigid beam fixed to a tripod. The Li samples were illuminated by an LED light source from outside the glove box (Amscope LED-50WY). Cross polarization was implemented to improve DIC.[30] The mechanical-testing system included a linear actuator (Newport TRB25CC), a force transducer (Futek LSB200, 2.2 N capacity), and custom 3D-printed grips for clamping the tensile specimens. All in-glove box experiments were conducted in displacement-control by setting the displacement rate of the actuator. A LabVIEW script controlled the position of the actuator, acquired the signal of the force transducer, and triggered the cameras.

Tensile specimens of Li were cut from foil strips with thickness of 0.75 ± 0.1 mm. The cutting was performed with a custom 3D-printed apparatus that clamped two flexible "feather" razor blades (Ted Pella) into an approximation of a dogbone shape, but with a continuous curvature, as illustrated schematically in Figure S1c. The minimum width of the undeformed gauge section had a value of 3.0 ± 0.1 mm, as illustrated in Figure S1a. A speckle pattern was then applied to these specimens for use with DIC. The speckle patterns were produced using a combination of MgO and graphite powders. First, the specimens were submerged in MgO powder, and gently agitated to promote adhesion of the MgO to the Li surface. Next, graphite powder was sprinkled over the surface through a 50 μm steel mesh to produce the speckles. This sequence of dark-on-light pigments reduces DIC error.[31] The graphite powder clumped on top of the MgO powder, and did not show evidence of reacting with the Li, based on SEM analysis (Figure S2).

The in-plane surface strains were measured by DIC with Vic3D 7 software (Correlated Solutions, Inc.). The camera system was calibrated with the calibration grid inside the glove box, and the cameras

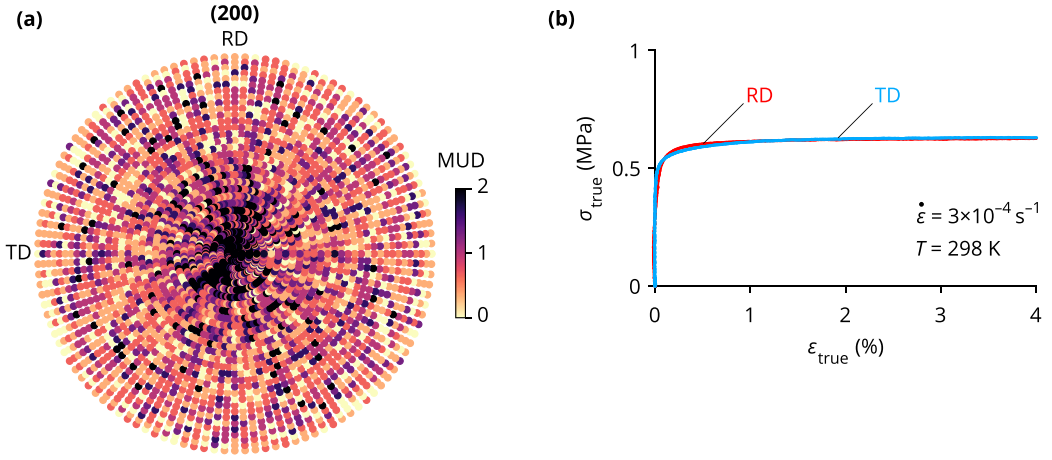

Figure 2. The crystallographic texture of the Li foil was measured by in-plane X-ray diffraction (a). In the (200) pole figure, no trend was found in the multiples of uniform distribution (MUD) with respect to in-plane rotation, indicating no differences in texture between the rolling direction (RD) and transverse direction (TD). Consistent with prior work,[29] the as-received Li foil had a preferential [100] texture in the normal direction to surface of the foil. Also, preliminary experiments with the in-glove box DIC system indicated similar tensile responses of samples with tensile axes in either the rolling direction (RD) or transverse direction (TD), as shown in (b).

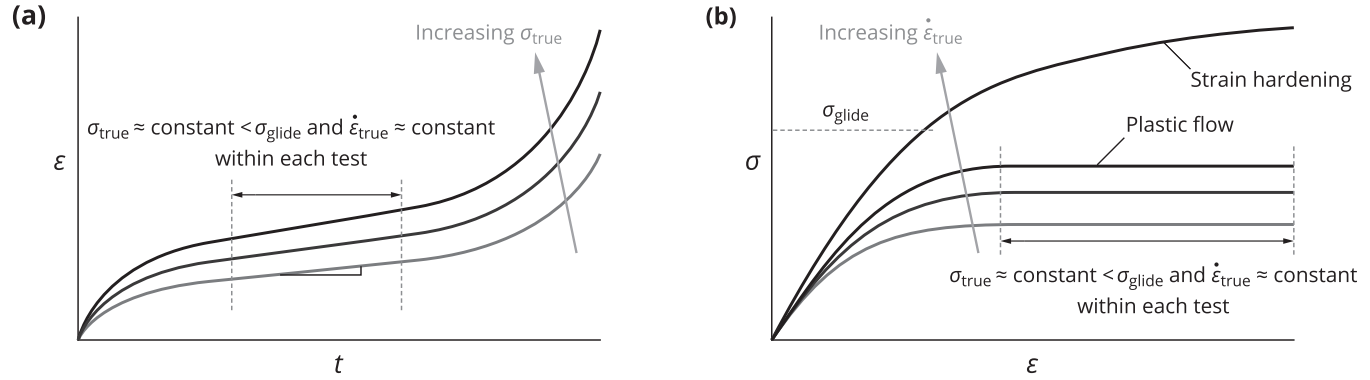

Figure 3. Under constant-force conditions, shown schematically in (a), steady-state conditions can be observed during secondary creep with the requirement that the temperature, true-strain rate ($\dot{\varepsilon}_{true}$) and true-stress (σ_{true}) are constant. During displacement-rate-controlled tension, shown schematically in (b), steady-state creep can also be observed at stresses below the glide stress, resulting in a constant flow stress that is strain-rate dependent. Under these conditions, the same conditions for steady-state creep (constant $\dot{\varepsilon}_{true}$ and σ_{true}) are observed.

were not re-positioned or disturbed between the beginning of the calibration and the end of the experiment. The correlation threshold parameters were 0.2 pixel consistency threshold, 0.5 pixel maximum confidence interval, and 1.0 pixel matchability threshold.

From the axial DIC strain maps, the data from a rectangular region over the middle of the gauge section was averaged to determine the nominal strain, ε_{nom}. To ensure a uniform strain profile and avoid strain-gradient effects, the height of the rectangular region was decreased until further reduction of the height did not change the average strain computation. The height at which this convergence was observed was 500 μm. The true strains were computed from the equation: $\varepsilon_{true} = \ln(1 + \varepsilon_{nom})$. True-strain rates were computed from the true strains and from the LabVIEW data-acquisition clock time. The nominal stress, σ_{nom}, was computed from the applied force, P, and the cross-sectional area of the Li in the inspected 500 μm rectangular region of the gauge section before deformation, A_o. Isochoric conditions for Levy-Mises flow were verified by noting that the negative transverse strains were half the axial strains for DIC data measured in the true-strain range of 5 to 25%. Therefore, the true stress was computed from the equation: $\sigma_{true} = \sigma_{nom}(1 + \varepsilon_{nom})$.

Methods for temperature-dependent measurements in inert gas environments.—A dynamic mechanical analyzer (DMA) with an environmental chamber (TA Instruments, RSA-G2, shown in Figure S3) was used to measure the effects of temperature on the deformation of the Li (Results of temperature-dependent deformation section). For the cooled experiments (198 to 248 K), the inert environment was chilled nitrogen gas evaporated from a liquid-nitrogen source. Reactions between Li and N_2 were not observed at the sub-ambient temperatures (Figure S3), as suggested by prior cryogenic transmission-electron microscopy showing that Li does not react with liquid N_2.[32] For the heated experiments (298 to 398 K), the inert environment was heated Ar gas. For both the cooled and heated conditions, oxidation/nitridation of the metal surface was not observed during the mechanical test, as shown by visual inspection (Figure S3).

The tensile experiments with the DMA were controlled with a custom Python script. The gauge length of the Li-foil specimens was 25 mm, with a width of 2–3 mm (Figure S3d). The samples were loaded in the grips at room temperature, and force control was used to maintain a stress of about 0 MPa during thermal expansion or contraction as the samples were heating or cooling, respectively, to the experimental temperature (Figure S4).

Results

Broadly, there are three important ways that metals deform: elasticity, plasticity, and creep. During reversible, *elastic* deformation, chemical bonds change length under stress and return to their original lengths when the stress is removed. Above a critical stress (yield strength), slip from dislocation glide gives rise to permanent, *plastic* deformation, and dislocation glide often leads to strain hardening. Along with glide, permanent deformation can also occur at stresses below the yield strength, as a result of *creep*. In contrast to dislocation glide, creep is less sensitive to stress and more sensitive to temperature. Consequently, creep results in a strain-rate dependent flow stress if the homologous temperature is high enough. Thus, creep deformation is expected to be important for Li even at room temperature because of its low melting temperature.

There are two main creep mechanisms in a metal: diffusional creep and power-law creep. Diffusional creep occurs at very low stresses as atoms diffuse between grain boundaries, and it is characterized by a linear relationship between stress and strain rate. Power-law creep dominates over diffusional creep at higher stresses, owing to its higher dependence on stress. Power-law creep occurs when the temperature is high enough for dislocations to be able to climb out of their glide plane and bypass obstacles. The uniaxial strain rate ($\dot{\varepsilon}$) is related to the uniaxial stress (σ) in power-law creep by the equation

$$\dot{\varepsilon} = A_c \sigma^m \exp\left(\frac{-Q_c}{\bar{R}T}\right), \quad [1]$$

where A_c is a material-specific creep parameter, m is the power-law creep exponent, Q_c is the activation energy for dislocation climb, $\bar{R}$ is the molar gas constant (8.31 J mol^{-1} K^{-1}), and T is the temperature. Our experimental results will be used to calibrate the material parameters (A_c, m, and Q_c) in Equation 1 for a power-law creep model.

Creep can be measured using constant-force or constant-stress experiments, by reporting strain as a function of time. Steady-state creep measurements require a constant temperature, a constant true-strain rate ($\dot{\varepsilon}_{true}$) and a constant true-stress (σ_{creep}). As illustrated schematically in Figure 3, these steady-state creep conditions may be observed with either constant-force or constant-displacement-rate experiments. In this work, both experimental approaches were used to achieve steady-state creep conditions over a wide range of strain rates.

This work will be presented in terms of these three mechanisms (elasticity, plasticity, and creep), with the observations being used to deduce the relevant material parameters for Li. In particular, it should be noted that at stresses below the yield strength, the deformation of Li is expected to have a contribution from the elastic strain and the creep strain. Except at very low temperatures or high strain rates, the creep strain is expected to be significant after relatively short periods of time. At low temperatures or high strain rates, it is possible for the stress levels to build up sufficiently quickly that eventually they are limited by plasticity, not steady-state creep, in which case, effects of strain hardening may be observed. It should be noted that with a low-melting temperature material such as Li, the effects of

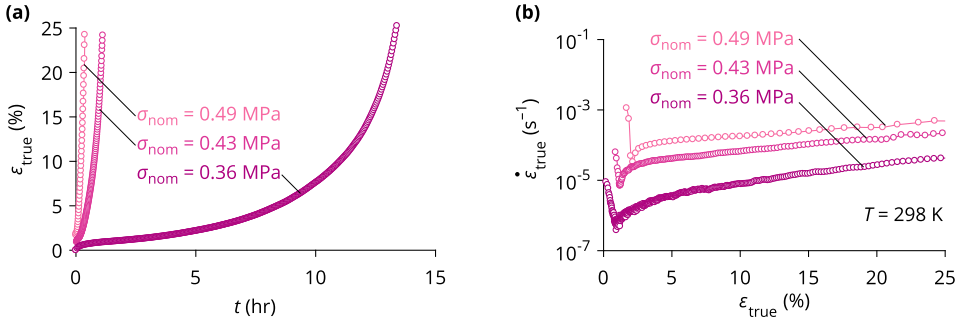

Figure 4. The creep curves of true strain ε_{true} versus time t at 298 K (a) for three nominal stresses (σ_{nom} = 0.36, 0.43, and 0.49 MPa). The glovebox-integrated DIC system shown in Figure S1 was used, but with a hanging weight that applied constant force to the Li foil. Average creep rates $\dot{\varepsilon}_{true}$ over the central 500 μm of the gauge section at a temperature of T = 298 K are shown in (b).

temperature on elastic modulus (elasticity), yield strength (plasticity), and creep rate (creep) may all be significant. For example, this has been noted by a discrepancy in reports of the elastic modulus of Li between pulse-echo techniques and mechanical tension/compression techniques, since tension/compression measurements of elasticity will be influenced by temperature- and rate-dependent, viscous effects.[33] Furthermore, the elastic modulus itself can have a temperature dependence in low-melting temperature materials, owing to the effects of thermal expansion on bond strength.[34]

Results of strain-rate dependent deformation.—As discussed earlier, Li creeps very easily, owing to its relatively low melting temperature. Therefore, the stress-strain behavior of Li is highly dependent on strain rate. To demonstrate this effect, constant-force and constant-displacement-rate tensile tests were performed on Li foil in Ar using the glovebox-integrated digital-image correlation (DIC) system shown in Figure S1. DIC is a non-contact surface deformation measurement technique that provides a field of displacements (Figure S1), in contrast with 1-D measurements from extensometers or strain gauges. This enabled strain mapping on the Li surface without chemically disturbing the samples.[35]

Constant-force experiments were conducted using the glovebox-integrated DIC system (Figure S1), with the load applied from a hanging weight. As shown in Figure 4, time-dependent deformation was observed, illustrating the importance of creep in Li at very low stresses and at room temperature. DIC also enabled measurement of true-strain rate ($\dot{\varepsilon}_{true}$). These constant force measurements did not begin to approach steady-state conditions until the true strain was between 10% and 20% (Figure 4b). Therefore, while constant-force measurements allow for observation of creep, constant-displacement-rate measurements were also performed to provide a more quantitative measure of steady-state creep at constant true-strain rates and constant true stresses.

Four tests were performed with different applied displacement rates, and the true stress is plotted against true strain in Figure 5a. The true-strain rates corresponding to these displacement rates were also computed from the DIC strains. As shown in Figure 5b, steady-state behavior was observed between strains of approximately 5 to 20%.

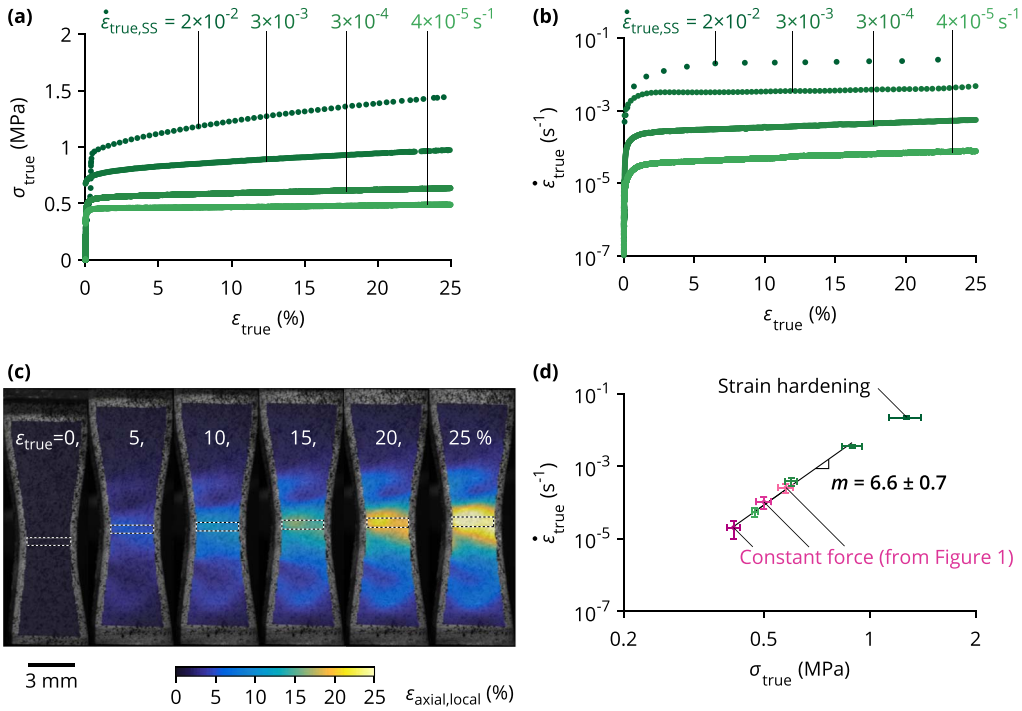

Figure 5. The mechanical responses of Li foil at 298 K are shown as true stress σ_{true} against true strain ε_{true} for steady-state true-strain rates between 4×10^{-5} and 2×10^{-2} s^{-1} (a). The measured true-strain rate $\dot{\varepsilon}_{true}$ versus ε_{true} indicated the regime of steady-state deformation was at ε_{true} between 5 and 20% (b). A sequence of axial strain maps from DIC ($\varepsilon_{axial,local}$) for the sample with 3×10^{-4} s^{-1} strain rate is shown (c). The rectangle from which DIC measurements were averaged is also shown. The true-strain rate $\dot{\varepsilon}_{true}$ is plotted against the true stress σ_{true} in (d), along with the constant-force measurements from Figure 4, to calibrate the power-law creep exponent ($m = 6.6 \pm 0.7$). The slope fitting excluded the fastest strain rate (2×10^{-2} s^{-1}), since it exhibited strain hardening. The uncertainty in the power-law creep exponent is the 95% confidence interval, and the error bars on the data in (d) represent the bounds of true-strain rate and true stress from the steady-state region of the experiments.

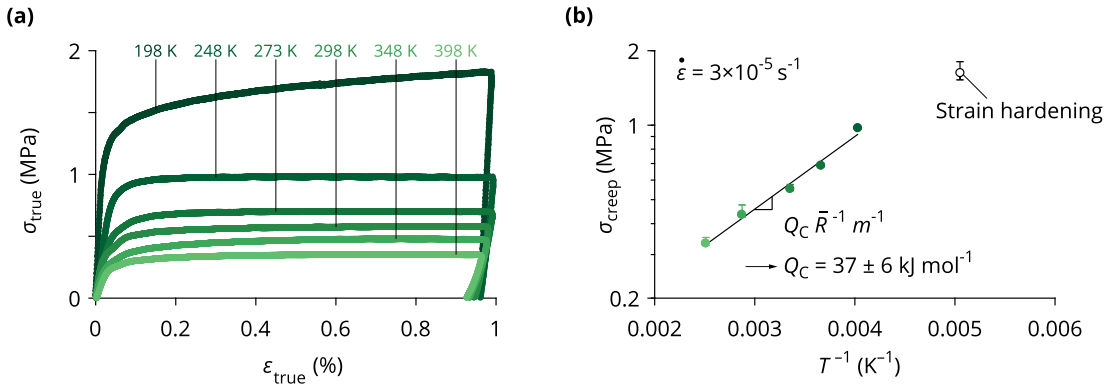

Figure 6. The temperature-dependent response of the Li foil was measured between 198 and 398 K at a strain rate of 3×10^{-5} s^{-1} (a). Strain hardening was observed only at the lowest temperature (198 K). For the other temperatures (≥248 K) where strain hardening was not observed, the creep activation energy (Q_c) and the creep parameter (A_c) were measured from the slope and intercept, respectively, of the logarithmic plot of creep stress (σ_{creep}) versus temperature (b). The error bars indicate the range of σ_{true} for each test between 0.2 and 1% true strain.

Within this steady-state range, the true-strain rates ($\dot{\varepsilon}_{true,SS}$) spanned from 4×10^{-5} to 2×10^{-2} s^{-1}. Significant strain hardening was observed only for the fastest strain rate (2×10^{-2} s^{-1}), while at lower strain rates, true stress remained essentially constant, indicating that creep was the dominant deformation mechanism over these ranges. Examples of the axial strain maps are provided in Figure 5c for the strain rate of 3×10^{-4} s^{-1}. As described in the Results of strain-rate dependent deformation section and indicated in Figure 5c, strains were computed from DIC measurements in the central 500 μm of the gauge section.

The power-law creep exponent (m) was calibrated from the true-strain rate versus stress data from the constant-force and constant-displacement-rate experiments (Figure 5d). The power-law creep exponent calculation excluded the fastest strain rate, where strain hardening was observed. The slope of this plot gives a value of $m = 6.6 \pm 0.7$. We note that this power-law creep exponent is consistent with earlier reports that were each conducted at room temperature.[18,20]

To assess the slight deviations from steady-state conditions in our experiments, error bars are provided in Figure 5d that correspond to the range of true-strain rate ($\Delta\dot{\varepsilon}_{true,SS}$) and the range of true stress ($\Delta\sigma_{true,SS}$) for the regions used to calibrate the creep model. The constant-force test with the slowest strain rate exhibited the largest range in true-strain rate ($\Delta\dot{\varepsilon}_{true,SS}$), indicated by the error bars on the test with the slowest strain rate in Figure 5d. Within this range of $\Delta\dot{\varepsilon}_{true,SS}$, the variation in computed power-law creep stress is below $\Delta\sigma_{true,SS} = 7\%$, following $\Delta\sigma_{true,SS} = (1/m)\Delta\dot{\varepsilon}$. This demonstrates the utility of this fit to describe the power-law creep behavior of Li over the range of strain rates presented.

Temperature-dependent deformation.—A power-law creep model was calibrated to incorporate the coupled roles of strain rate and temperature on Li deformation. The creep stress (σ_{creep}) can be expressed by rearranging Equation 1, with

$$\sigma_{creep} = \left(\frac{\dot{\varepsilon}}{A_c}\right)^{1/m} \exp\left(\frac{Q_c}{m\bar{R}T}\right) . \qquad [2]$$

The quantity $A_c \exp(-Q_c/\bar{R}T)$ in Equation 1 can be computed from the data of Figure 5d as ≈ 0.01 MPa^{-m} s^{-1}, where m is the power-law creep exponent. However, as described below, creep rates as a function of temperature need to be measured to split this term into a useful expression that will capture the effects of temperature. To accomplish this, uniaxial tensile tests were conducted between 198 and 398 K at nominal strain rates of 3×10^{-5} s^{-1} for strains up to 1% (Figure 6). From these plots, it is observed that the true stress reaches a plateau (creep stress) at this strain rate for temperatures ≥ 248 K. If this value of creep stress is plotted against the inverse temperature, as shown in Figure 6b, an activation energy for dislocation climb of $Q_c = 37 \pm 6$ kJ mol^{-1} is obtained. The calculation of this activation energy excluded the test at 198 K, since it exhibited strain hardening. This value can be compared with a quoted value of about 50 kJ mol^{-1} for lattice diffusion.[12,18] While diffusion through the lattice is one mechanism for climb, it is also noted that core-diffusion is another possible mechanism, which is expected to have a lower activation energy. The creep constant was measured as $A_c^{-1/m} = 3.0 \times 10^5 \pm 5.5 \times 10^4$ s^{-1} Pa.

Table I presents the calibrated parameters for power-law creep and their 95% confidence intervals. The power-law creep exponent (m) was calibrated in Figure 5, and the creep activation energy (Q_c) and creep parameter (A_c) were calibrated in Figure 6. The predicted creep stress from Equation 2 is shown in Figure 7. Thus, based on these observations, we propose a simple constitutive model of bulk Li deformation as elastic-viscoplastic at strain rates below approximately 10^{-3} s^{-1}, with a creep stress determined by this power-law creep relationship. These parameters capture the strain-rate- and temperature-dependent viscoplasticity of bulk polycrystalline Li, which can be

Table I. The calibrated material parameters for the Li power-law creep model in Equation 2. The uncertainties with each calibrated parameter are the 95% confidence intervals from the T-distribution.

m	Q_c (kJ mol^{-1})	$A_c^{-1/m}$ (s^{-1} Pa)
6.6 ± 0.7	37 ± 6	$3.0 \times 10^5 \pm 5.5 \times 10^4$

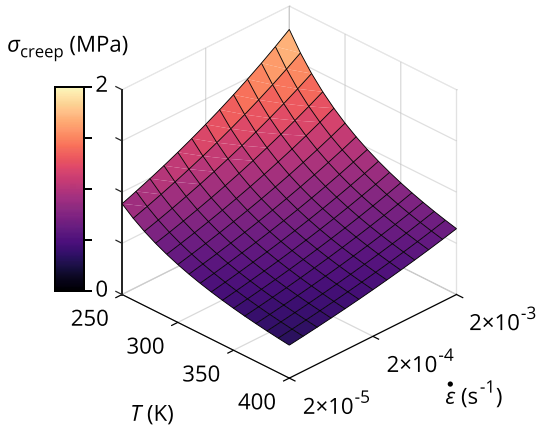

Figure 7. The creep stress for the power-law model's valid range of 248 to 398 K and 2×10^{-5} to 2×10^{-3} s^{-1}.

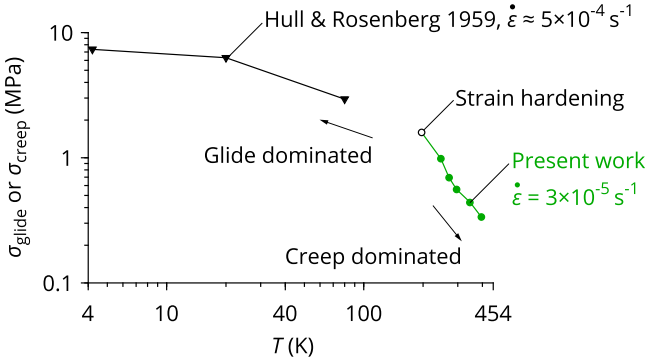

Figure 8. When compared with the yield stress of Li at cryogenic temperatures,[14] there is a transition from creep-dominated to glide-dominated deformation.

used to build upon modeling efforts including the three-dimensional, large-deformation, elastic-viscoplastic model for Li described by Narayan and Anand.[27]

Transition to strain hardening.—The data acquired at temperatures ≥248 K in Figure 6 are clearly consistent with a creep mechanism. However, the stress-strain curve at the lowest temperature (198 K) appears to show some effects of strain hardening. This low-temperature, high-stress behavior is consistent with standard models of creep and plasticity, where glide dominates if the stresses reach high-enough levels. In this context, the present work makes a connection with cryogenic measurements of Li yield by Hull and Rosenberg.[14] As shown in Figure 8, the yield strength measured at low temperatures is temperature sensitive. Along with the observation of strain hardening for the fastest strain rate in Figure 5, this suggests the transition from creep-dominated to glide-dominated deformation for lower temperatures (<248 K) and faster strain rates ($>2 \times 10^{-3}$ s^{-1}).

Discussion

Electrochemical-mechanical coupling with current density.—As these results illustrate, creep effects in Li-metal batteries could be significant over a wide range of current densities and operating conditions. As a simplified example, under the assumption of uniform and unconstrained plating over an area A on a Li anode with height h, the amount of Li plated over an increment of time dt corresponds to a change in height dh (Figure 9a). However, in practical battery formats, a stack pressure is always applied, and Li electrodeposition is constrained by the surrounding materials. This induces compression during electrodeposition, which can be clearly observed in the flattened morphology of mossy dendrites deposited within a coin cell in Effects of constrained boundaries and stack pressure on Li morphology section. As an upper bound of this behavior, if the boundary conditions of the surrounding materials (current collector, separator/electrolyte, etc.) are rigid, the equivalent true-strain rate during this plating is

$$\dot{\varepsilon} = \frac{1}{h}\frac{dh}{dt} . \qquad [3]$$

Following Faraday's law, the rate of the electrochemical reaction dN/dt is proportional to the current I (or the current density J across area A), with

$$I = JA = zF\frac{dN}{dt} , \qquad [4]$$

where F is Faraday's constant, and the valence number of Li^+ is $z = 1$. By rearranging Equations 3 and 4 for dt and equating, the current density J is proportional to strain rate $\dot{\varepsilon}$, following

$$\dot{\varepsilon} = \left(\frac{JA}{hF}\right)\left(\frac{dh}{dN}\right) . \qquad [5]$$

The current density J is also proportional to the anode height, following

$$h = \left(\frac{JA}{\dot{\varepsilon}F}\right)\left(\frac{dh}{dN}\right) . \qquad [6]$$

For uniformly-plated Li, the term $A \times dh/dN$ is equal to the molar volume of Li (13 cm^3/mol at 298 K).

In Figure 9b, the current densities (J), heights (h), and corresponding strain rates ($\dot{\varepsilon}$) are provided with the regions where power-law creep and glide are dominant at 298 K. For a typical current density of $J = 1$ mA cm^{-2}, the minimum height for power-law creep is $h = 0.67$ microns.

Of course, there are limitations to this simplified electrochemical-mechanical relationship, but this basic scenario contextualizes the interplay between current density and strain rate. In practical battery systems, there are not perfectly rigid boundaries around the anodes, and there will be some strain accommodation in the surrounding materials that could be a function of electrolyte phase (solid and/or liquid), viscoelasticity in a polymer separator, strain effects in the cathode, and stack pressure. We note that this would lead to a decrease in strain rate, which would enhance the effects of creep relative to strain-hardening,

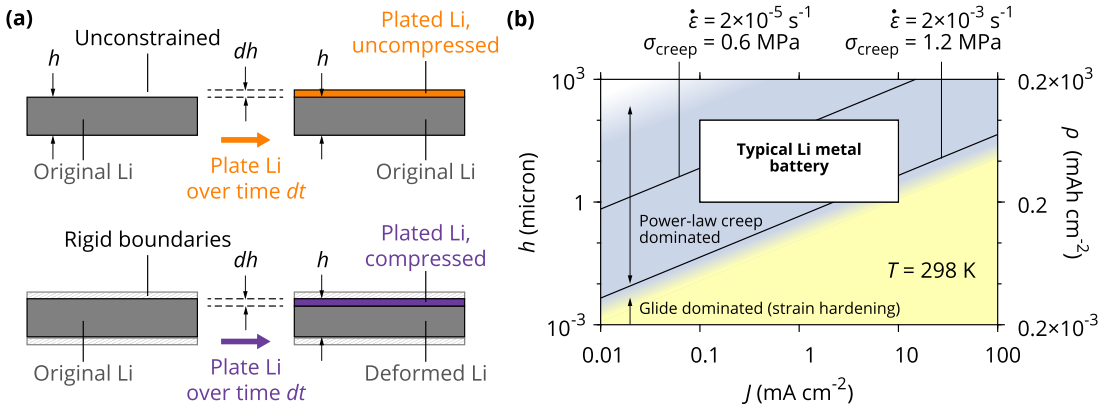

Figure 9. (a) For uniform Li deposition in an unconstrained cell, the plated Li forms without compression. For typical batteries, however, stack pressure is applied with constraints that can be approximated as rigid boundaries. Under these constrained conditions, the plated Li is compressed. (b) Plot of Li-metal height (h) versus current density of plating (J), indicating the dominant deformation mechanism. Lines of constant strain rate $\dot{\varepsilon}$ are plotted, and the transition from creep to strain hardening is indicated at 298 K. A regime for typical Li metal batteries is shown, assuming a practical range of J between 0.1 and 10 mA cm^{-2} and a Li anode height h of 1 to 100 μm.

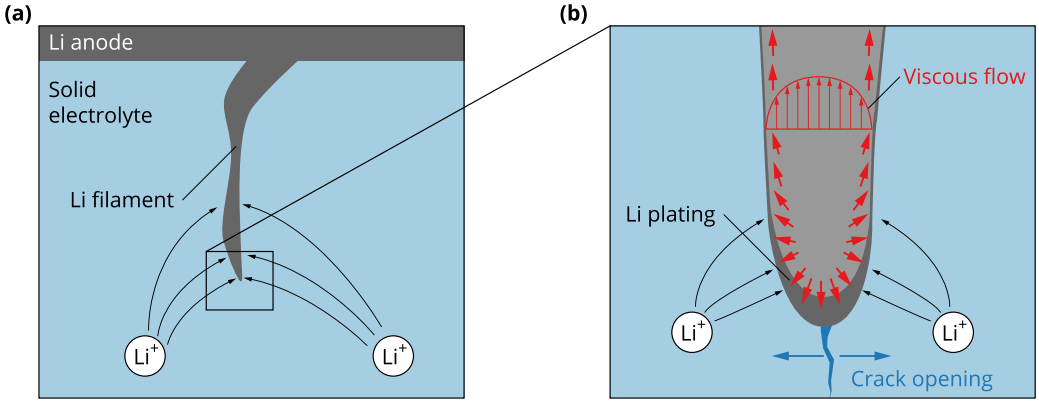

Figure 10. (a) In ceramic solid electrolytes, Li can penetrate into surface flaws, forming a filament.[5] (b) Stress accumulates at the tip of the Li filament as a function of current density, while there is viscous flow with a boundary layer away from the tip.

thereby extending the range of validity of this model to higher current densities.

Additionally, Li is known to plate inhomogeneously under many conditions, so localized strain (and strain rate) could vary under non-planar electrodepositon. In this case, the local strain rate could be higher than predicted in this simplified model, since only a fraction of the total electrode surface area is associated with Li plating.[3] However, as shown by operando video microscopy, this fractional surface area of plated Li rapidly increases as high surface area Li deposits grow,[3] and current focusing would have to be extremely localized to increase strain rate by greater than an order of magnitude.

The relationship between strain rate and current density above also assumes tension-compression symmetry in the Li stress-strain response (by extending the tensile measurements in this present work to a scenario of compression in this simplified model). This is a reasonable assumption, as tension-compression asymmetry would be abnormal in a body-centered cubic metal such as Li.

Furthermore, while Figure 9b presents relevant battery conditions at room temperature, the deformation of Li has significant temperature dependence, as shown in Figure 6. At temperatures above 298 K, the maximum strain rate (and corresponding maximum current density) for creep-dominated deformation in Figure 9b would increase. Typical operating temperatures for Li-metal batteries could vary between <243 K for space and defense applications,[36] to 353 K for high-power applications. Additionally, one of the widely-stated benefits of ceramic electrolytes is the reduced need for thermal management systems in transportation applications, which could lead to significant temperature variations.[37,38] These temperature-dependent properties should be taken into account in coupled electrochemical-mechanical modeling. For example, from 243 K and 353 K, the creep stress from Equation 2 would decrease by a factor of 2.4 for a given strain rate.

Creep effects on Li-polymer interfaces.—A series of publications has discussed the impacts of Li mechanics when interfaced with a solid polymer. This has implications for dendrite propagation both through polymer separators typically used in Li-ion batteries, as well as solid-state batteries incorporating polymer electrolytes. The original analysis by Monroe and Newman assumes that Li behaves as a linear-elastic solid, under which assumption the propagation of dendrites is proposed to be affected by the shear modulus of the polymer.[10] As shown in this study, the pertinence of linear-elastic models of coupled electrochemical-mechanical behavior is bound by small stresses (well below the yield strength of Li), and is also affected by temperature and strain rate.

Subsequent models have built upon the foundation of the Monroe-Newman model to incorporate plasticity using a strain-hardening model.[4,11] However, in the current work, we only observe strain hardening for relatively fast strain rates or low temperatures, indicating that creep (not strain hardening from glide) dominates Li deformation over a wide range of battery-relevant conditions. Recently, Goyal and Monroe included the framework for viscous effects in a thermodynamic model that provides a basis for future modeling efforts.[39] The present work provides the experimental properties of Li that could be incorporated in such future models.

Creep effects on ceramic electrolyte penetration.—One example of the role of Li mechanics is crack propagation through a brittle ceramic electrolyte. For example, in "superionic" solid electrolytes such as $Li_7La_3Zr_2O_{12}$, a critical current density is often observed, above which internal shorting occurs.[6,40] Following the model of Porz, et al.,[5] during Li plating at the anode-electrolyte interface, surface cracks can fill with plated Li. This can, in turn, lead to stresses that buildup at crack tips, which can drive brittle fracture of the solid electrolyte (Figure 10). The localized strain rate within the crack tip is expected to increase with current density, which would influence the stress accumulation within the crack. To expand upon this model, incorporation of creep could play an important role on the current-density dependence of localized mechanical deformation, which determines the trade-offs between localized viscous flow out of the crack, and development of stress at the crack tip (Figure 10b). We note that for nanoscale cracks, length-scale effects could also influence the mechanical properties of Li, as observed by recent nanomechanical studies of Li.[21–25] Furthermore, friction and surface adhesion effects would be expected to influence the extrusion and compression of Li in the crack, as has been recently discussed in the Li-$Li_7La_3Zr_2O_{12}$ system.[20,41]

Furthermore, temperature effects on the deformation of Li will affect solid-state batteries. For example, in the model by Porz, et al.,[5] current focusing at a crack tip is assumed. This could lead to non-uniform thermal distributions from Joule heating. A similar effect was recently modeled for the temperature rise of Li dendrites in liquid electrolytes,[42] and such effects could be amplified in ceramic electrolytes with lower thermal conductivities. Macroscopic temperature fluctuations will also contribute to the creep of Li, which could influence the rate of Li extrusion out of the crack, and therefore impact critical current density. This is consistent with the observation that the critical current density in $Li_7La_3Zr_2O_{12}$ increases with increasing cell temperature.[43] However, since multiple factors, including interfacial kinetics and ionic transport within the electrolyte, are also a function of temperature, a full mechanistic understanding of the coupled electrochemical-mechanical behavior of ceramic electrolytes requires further investigation.

Effects of constrained boundaries and stack pressure on Li morphology.—In addition to solid-state batteries, Li plating in liquid electrolytes often results in a variety of non-planar morphologies

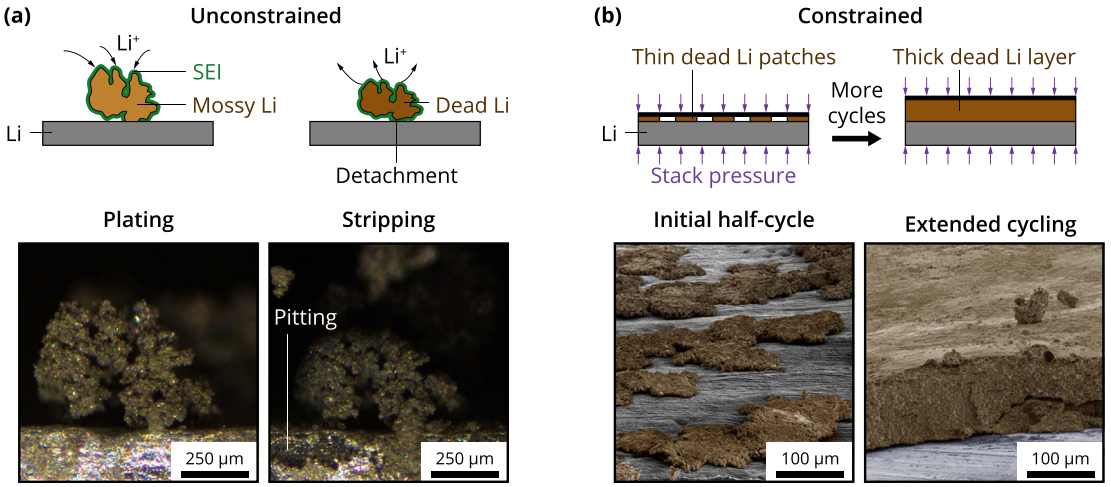

Figure 11. Operando optical microscopy of mossy Li dendrites without stack pressure, showing dead Li formation during stripping (a). SEM images of dead Li after coin cell disassembly, showing flat patches after the initial half-cycle and accumulation of a thick porous layer after extended cycling (b).

commonly referred to as "dendrites." For example, depending on variables including electrolyte composition, current density, and the electrode surface, a variety of "needle-like," "mossy," and "fractal" dendrite morphologies have been observed.[2] However, the impacts of plasticity and creep on the dynamic evolution of dendrite morphology when plating or stripping have not been fully described.

For example, operando video microscopy experiments have shown that without the presence of external mechanical pressure, mossy Li dendrites are unconstrained and grow out from the Li,[3] as shown in Figure 11a. However, when constrained within a coin cell, a flattened morphology is observed, demonstrating that the effects of constraints from stack pressure and the surrounding materials induce a significant compressive stress during growth. The final morphology of these compressed geometries will depend on variables including strain rate and temperature. Furthermore, upon Li dissolution, active Li is removed from the mossy dendrites, which causes large volume changes that can result in a complex three-dimensional stress distribution. As a result, metallic Li can become physically detached and/or electrically isolated. This leads to "dead Li" formation, which is critical to the overall cell performance since it contributes to low Coulombic efficiency. After extended cycling, dead Li accumulation (Figure 11b) leads to a tortuous, electrochemically inactive surface layer that hinders mass transport, eventually leading to cell failure.[7]

Despite these general observations, little is known about the impacts of Li mechanics on: 1) the morphological evolution of mossy Li, and how this is affected by Li viscoplasticity, stack pressure, and SEI mechanical properties; 2) the mechanical origins of dead Li formation; and 3) the role of viscoplasticity on the formation of the compact dead-Li layer on the surface, and how this relates to porosity and tortuosity of the surface layer. All of these phenomena will be affected by the temperature and strain rate (linked to current density) dependence of Li deformation.

Applications of Li viscoplasticity on Li-metal anode surface protection strategies.—Multiple groups have demonstrated that thin protective coatings can increase Li-metal battery performance.[8,44–46] In some cases, protective layers may fail mechanically during the manufacturing of the battery as a result of large-scale deformations of Li. To demonstrate this, an alumina protective layer was deposited on Li by atomic layer deposition (ALD). After assembly and disassembly in a coin cell (with no cycling), cracks on the order of one micron wide were observed in the ALD film (Figure 12), which resulted from the lateral expansion of the Li. This warrants further investigation of the role of viscoplastic Li deformation on surface protection layers, both during cell assembly and cycling. These observations, when combined with the present work's model of Li mechanics (Results of temperature-dependent deformation section), could inform strategies to tailor superior protective layers.

Conclusions

In this work, we have measured the mechanical response of Li in inert gas environments over a wide range of strain rates and temperatures. A power-law creep model was calibrated to predict Li deformation as a function of strain rate and temperature. We describe the general relationship between strain rate and current density, illustrating that power-law creep is the dominant deformation mechanism over a wide range of battery-relevant conditions. These results were connected with important topics in Li-metal batteries, including electrochemical-mechanical modeling of Li/solid interfaces, ceramic

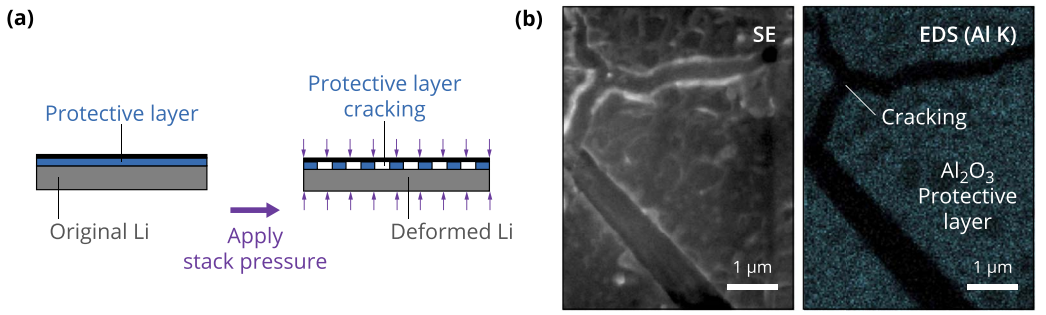

Figure 12. Stack pressure during cell assembly can deform Li and fracture its protection layer (a). For an alumina film produced with atomic layer deposition, cracks were observed in the film in secondary electron (SE) micrograph and Al K energy-dispersive X-ray spectroscopy (b).

electrolyte penetration, "dead Li" formation, and protective layers on Li anodes.

Acknowledgments

This material is based upon work supported by the National Science Foundation under grant No. 1751590. The authors thank Prof. Samantha Daly, Prof. John Shaw, and Prof. Kevin Wood for insightful discussions; Reo Kimachi (Keio University) for language translation of a work in Japanese;[19] and Callan Luetkemeyer and John Weeks for insights and assistance to develop the powdered speckle patterning method for DIC. The authors declare no competing interests.

ORCID

William S. LePage https://orcid.org/0000-0002-6811-3162
Neil P. Dasgupta https://orcid.org/0000-0002-5180-4063

References

1. D Lin, Y. Liu, and Y. Cui, *Nature Nanotech.*, **12**(3), 194 (2017).
2. K. N. Wood, M. Noked, and N. P. Dasgupta, *ACS Energy Letters*, **2**, 664 (2017).
3. K. N. Wood, E. Kazyak, A. F. Chadwick, , K.-H. Chen, J.-G. Zhang, K. Thornton, and N. P. Dasgupta, *ACS Central Science*, **2**(11), 790 (2016).
4. P. Barai, K. Higa, and V. Srinivasan, *Phys. Chem. Chem. Phys.*, **19**(31), 20493 (2017).
5. L. Porz, T. Swamy, B. W. Sheldon, D. Rettenwander, T. Frömling, H. L. Thaman, S. Berendts, R. Uecker, W. C. Carter, and Y. M. Chiang, *Advanced Energy Materials*, **7**(20) (2017).
6. A. Sharafi, H. M. Meyer, J. Nanda, J. Wolfenstine, and J. Sakamoto, *Journal of Power Sources*, **302**, 135 (2016).
7. K.-H. Chen, K. N. Wood, E. Kazyak, W. S. LePage, A. L. Davis, A. J. Sanchez, and N. P. Dasgupta, *Journal of Materials Chemistry A: Materials for energy and sustainability*, **5** (2017).
8. A. C. Kozen, C.-F. Lin, O. Zhao, S. B. Lee, G. W. Rubloff, and M. Noked, *Chemistry of Materials*, **29**(15), 6298 (2017).
9. Department of Energy Office of Science, Next Generation Electrical Energy Storage Basic Research Needs (BRN) Workshop, (2017).
10. C. Monroe and J. Newman, *Journal of The Electrochemical Society*, **152**(2), A396 (2005).
11. P. Barai, K. Higa, and V. Srinivasan, *Journal of The Electrochemical Society*, **165**(11), A2654 (2018).
12. R. Messer and F. Noack, *Applied Physics*, **6**(1), 79 (1975).
13. F. Hao, A. Verma, and P. P. Mukherjee, *ACS Applied Materials & Interfaces*, **10**(31), 26320 (2018).
14. D. Hull and H. M. Rosenberg, *Philosophical Magazine*, **4**(39), 303 (1959).
15. I. Gorgas, P. Herke, and G. Schoeck, *Physica Status Solidi (a)*, **67**(2), 617 (1981).
16. R. Schultz, *Lithium: Measurement of Young's modulus*, Tech. rep., Fermilab, (2002).
17. S. Tariq, K. Ammigan, P. Hurh, R. Schultz, P. Liu, and J. Shang, *Particle Accelerator Conf.*, 1452 (2003).
18. P. M. Sargent and M. F. Ashby, *Scripta Metallurgica*, **18**, 145 (1984).
19. S. Hori, K. Saito, and T. Hasegawa, *Journal of Japan Institute of Light Metals*, 660 (2000).
20. A. Masias, N. Felten, R. Garcia-Mendez, J. Wolfenstine, and J. Sakamoto, *Journal of Materials Science*, **54**(3), 2585 (2019).
21. Y. Wang and Y.-T. Cheng, *Scripta Materialia*, **130**, 191 (2017).
22. E. G. Herbert, S. A. Hackney, N. J. Dudney, and P. S. Phani, *Journal of Materials Research*, **33**(10), 1335 (2018).
23. E. G. Herbert, S. A. Hackney, V. Thole, N. J. Dudney, and P. S. Phani, *Journal of Materials Research*, **33**(10), 1347 (2018).
24. E. G. Herbert, S. A. Hackney, V. Thole, N. J. Dudney, and P. S. Phani, *Journal of Materials Research*, **33**(10), 1361 (2018).
25. C. Xu, Z. Ahmad, A. Aryanfar, V. Viswanathan, and J. Greer, *Proceedings of the National Academy of Science*, **114**(1), 1 (2016).
26. C. Campbell, Y. M. Lee, K. Y. Cho, Y.-G. Lee, B. Lee, C. Phatak, and S. Hong, *Scientific reports*, **8**(1), 2514 (2018).
27. S. Narayan and L. Anand, *Extreme Mechanics Letters*, **24**, 21 (2018).
28. F. Bachmann, R. Hielscher, and H. Schaeben, Texture analysis with MTEX - free and open source software toolbox. In Solid State Phenomena, *Trans Tech Publ*, **160**, 63 (2010).
29. F. Shi, A. Pei, A. Vailionis, J. Xie, B. Liu, J. Zhao, Y. Gong, and Y. Cui, *Proceedings of the National Academy of Sciences*, **114**(46), 12138 (2017).
30. W. LePage, S. Daly, and J. Shaw, *Experimental Mechanics*, **56**(6), 969 (2016).
31. W. LePage, J. Shaw, and S. Daly, *Experimental Techniques*, **41**(5), 557 (2017).
32. Y. Li, Y. Li, A. Pei, K. Yan, Y. Sun, C.-L. Wu, L.-M. Joubert, R. Chin, A. L. Koh, Y. Yu, J. Perrino, B. Butz, S. Chu, and Y. Cui, *Science*, **358**(6362), 506 (2017).
33. S. Yu, R. D. Schmidt, R. Garcia-Mendez, E. Herbert, N. J. Dudney, J. B. Wolfenstine, J. Sakamoto, and D. J. Siegel, *Chemistry of Materials*, **28**(1), 197 (2015).
34. H. J. Frost and M. F. Ashby, *Deformation-mechanism maps: the plasticity and creep of metals and ceramics*, Pergamon Press, (1982).
35. E. Jones, M. Silberstein, S. R. White, and N. R. Sottos, *Experimental Mechanics*, **54**(6), 971 (2014).
36. C.-K. Huang, J. Sakamoto, J. Wolfenstine, and S. Surampudi, *Journal of the Electrochemical Society*, **147**(8), 2893 (2000).
37. Z. Zhang, Y. Shao, B. V. Lotsch, Y.-S. Hu, H. Li, J. Janek, C. Nan, L. Nazar, J. Maier, and M. Armand, et al., *Energy & Environmental Science*, **11**, 1945 (2018).
38. J. Schnell, T. Günther, T. Knoche, C. Vieider, L. Köhler, A. Just, M. Keller, S. Passerini, and G. Reinhart, *Journal of Power Sources*, **382**), 160 (2018).
39. P. Goyal and C. W. Monroe, *Journal of The Electrochemical Society*, **164**(11), E3647 (2017).
40. A. Sharafi, E. Kazyak, A. L. Davis, S. Yu, T. Thompson, D. J. Siegel, N. P. Dasgupta, and J. Sakamoto, *Chemistry of Materials*, **29**(18), 7961 (2017).
41. M. Wang and J. Sakamoto, *Journal of Power Sources*, **377**, 7 (2018).
42. L. Li, S. Basu, Y. Wang, Z. Chen, P. Hundekar, B. Wang, J. Shi, Y. Shi, S. Narayanan, and N. Koratkar, *Science*, **359**(6383), 1513 (2018).
43. N. J. Taylor, S. Stangeland-Molo, C. G. Haslam, A. Sharafi, T. Thompson, M. Wang, R. Garcia-Mendez, and J. Sakamoto, *Journal of Power Sources*, **396**, 314 (2018).
44. E. Kazyak, K. N. Wood, and N. P. Dasgupta, *Chemistry of Materials*, **27**(18), 6457 (2015).
45. N.-W. Li, Y.-X. Yin, C.-P. Yang, and Y.-G. Guo, *Advanced Materials*, **28**(9), 1853 (2016).
46. L. Chen, J. G. Connell, A. Nie, Z. Huang, K. R. Zavadil, K. C. Klavetter, Y. Yuan, S. Sharifi-Asl, R. Shahbazian-Yassar, and J. A. Libera, et al., *Journal of Materials Chemistry A*, **5**(24), 12297 (2017).